ELSEVIER

Nuclear Instruments and Methods in Physics Research A 430 (1999) 245–259

NUCLEAR INSTRUMENTS & METHODS IN PHYSICS RESEARCH Section A

www.elsevier.nl/locate/nima

Design principles of the end cap drift chambers in the L3 experiment

V. Andreev, G. Gavrilov, A. Krivshich*, V. Maleev, A. Nadtochy, S. Patrichev, S. Volkov

Petersburg Nuclear Physics Institute, Russia Academy of Science, High Energy Physics Division, 188350 Gatchina, St. Petersburg, Russia

Received 25 June 1997; received in revised form 24 January 1999

Abstract

The end cap detector based on multimodule construction has been designed and produced for the L3 experiment. The purpose of this article is to present a fruitful approach for solving the complex problem of selecting a set of strongly interrelated design parameters to satisfy performance criteria in the face of severe environmental and space constraints. The design principle of the end cap drift chamber affected by a complex of external problems caused by the layout is reviewed. It is shown that in the framework of detailed consideration of each parameter, a good space–time linearity, spatial and angular resolution is obtainable. The results of experimental tests are presented. © 1999 Elsevier Science B.V. All rights reserved.

Keywords: End cap detector; Design principle; L3 experiment

1. Introduction

The L3 central detector end cap Forward Tracking Chambers (FTC) were designed to cover the forward/backward region in the range of polar angle $8^\circ \leq \theta \leq 35^\circ$ to the beam axis Z (see Fig. 1a). The need for this detector was caused by insufficient resolution of the Z - detector of the L3 central time expansion chamber (TEC) ($\sigma \approx 0.8$–1 mm) for particles at these forward angles [1]. Secondly, multiple scattering in the TEC's thick external flange (13 g/cm^2) made it necessary to remeasure more exactly the particle tracks entering the electromagnetic BGO calorimeter (EMC). These requirements led to the following specifications for the FTC detector:

- detection of charged particles and measurement of the location and direction of their tracks with spatial resolution of $\sigma \leq 150$ μm and angular resolution better than 10 mrad;
- determination of the track multiplicity originating from the interaction region for up to 5–7 particles passing the FTC;
- the detector was intended to operate with no service access for about 2–3 yr;
- the thickness of the detector along the beam axis could not be more than 72 mm;
- the heat dissipation from the FTC electronics and high-voltage dividers was limited to 50 W

* Corresponding author. Tel.: + 7-812-71-46046, fax: + 7-812-71-37976.

E-mail address: kriv@rec03.pnpi.spb.ru (A. Krivshich)

0168-9002/99/$ - see front matter
PII: S0168-9002(99)00201-6

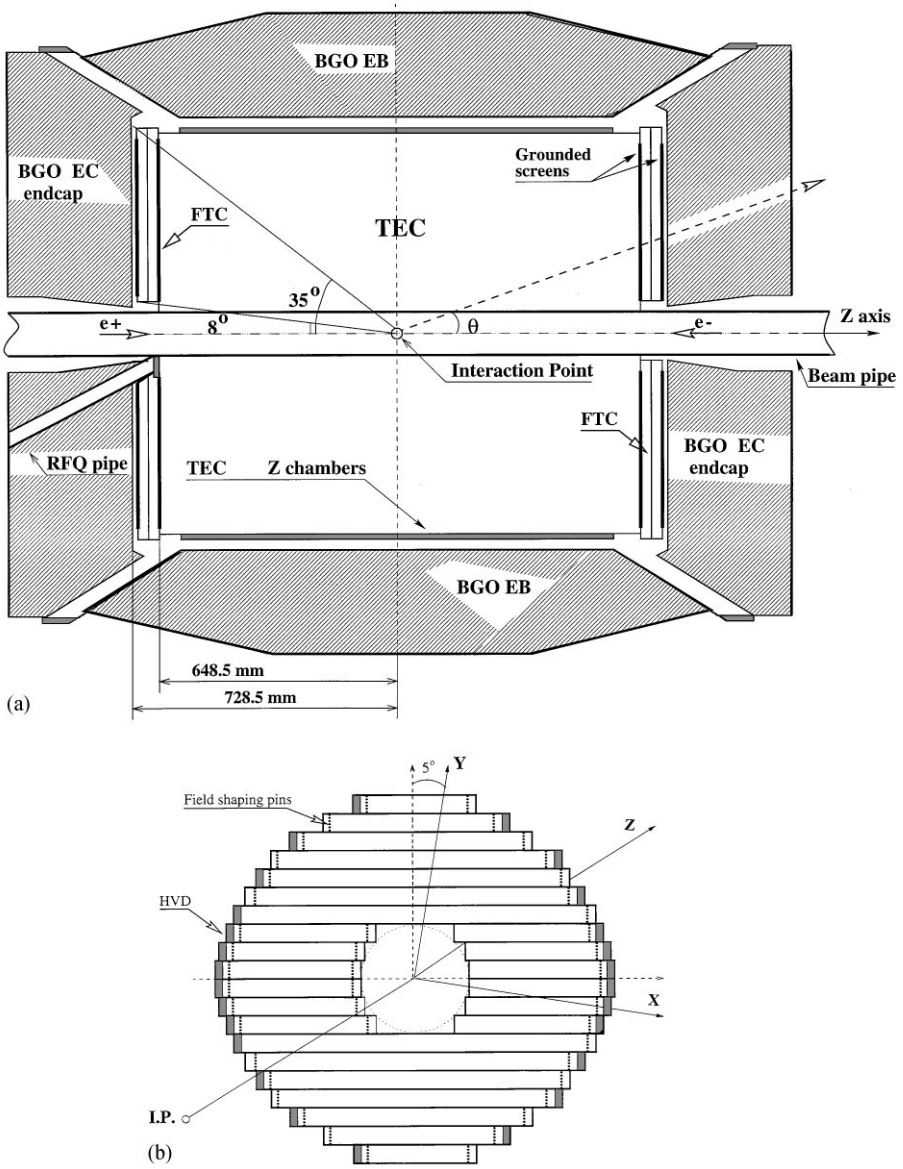

Fig. 1. Schematic view of the FTC layout. (a) Location between the BGO calorimeter and TEC central detector, (b) FTC layer front view, it is seen that the local orthogonal coordinate system of the FTC layer is turned at $\varphi = 5^\circ$ with respect to the global system of coordinates.

per end cap by the proximity of the nearest electromagnetic calorimeter electronics and poor convection conditions.

The realization of these goals was severely constrained by the limited space available for the detector between the electromagnetic calorimeter and the central detector. For the sake of reliability we chose the multimodule construction of independent drift chambers. We could not employ a version of the proportional chamber with cathode readout as it would have needed

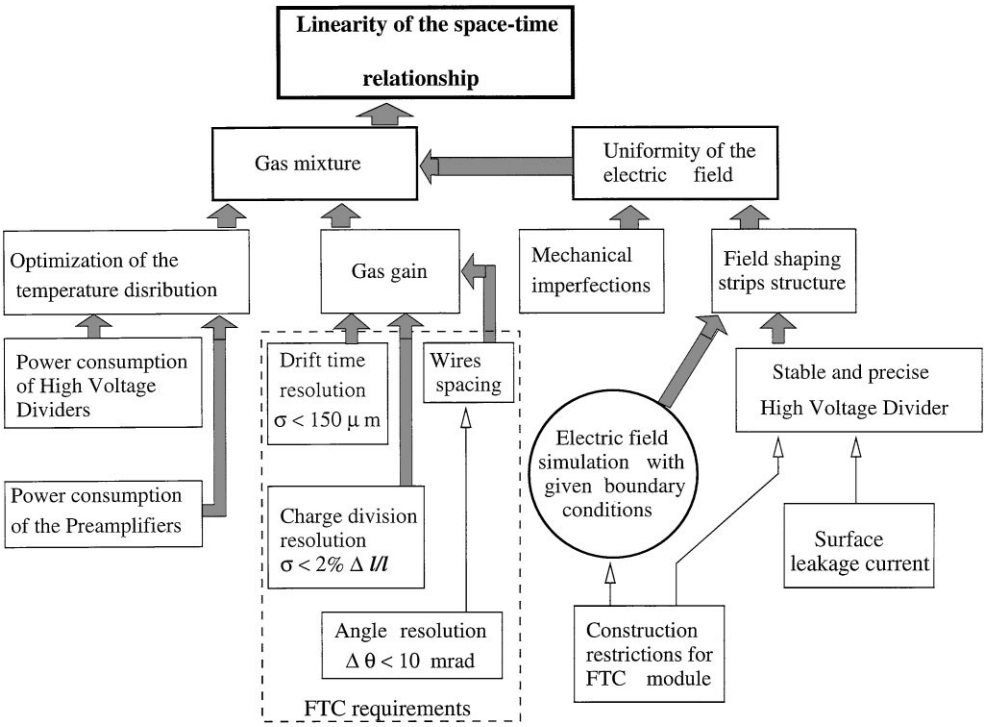

Fig. 2. Scheme of the relationship between the design parameters affecting the space–time linearity of the FTC.

too much space for readout electronics and cabling.

To achieve the necessary FTC characteristics satisfying the reliability demands, we were obliged to find consistent solutions to a complex of related problems affecting both the space–time dependence and the spatial resolution of the drift chamber. The relationship between the design parameters affecting the space-time linearity of the FTC is presented in Fig. 2. Our main goal was to optimize each of the FTC design parameters so as to provide the differential nonlinearity of the space–time (Y–T) relation (absolute measurement of the particle coordinate) at the level of better than 70 μm for any wire of the drift module.

The proximity of the FTC with the TEC and BGO required a reliable electrical protective screen from these noise sources, as was done in Ref. [2]. As was shown in Refs. [3,4], the electric field in the drift cells in such a situation is distorted and the relationship between the drift time and coordinates of the particles becomes nonlinear. This is one example of how space limitation makes the required performance difficult to achieve, in this case through the influence of the external protection grounded screens on the electric field structure in the FTC modules. It was found possible to compensate the deleterious effects of the screen through a careful choice of both the geometry and potentials of the field shaping electrodes of the FTC.

The high track multiplicity required that each module redundantly determine the coordinates of the tracks – via drift time with high resolution and via charge division with moderate resolution. This restricted the choice of gas mixture to those with a saturated plateau of electron drift velocities, for good $Y-T$ linearity as well as high enough gas gain for charge division measurements.

Poor ambient convection conditions in the FTC region can cause temperature gradients in the gas mixture due to the local overheating of module surfaces by the heat-radiating components. This is

also a factor capable of distorting the $Y-T$ linearity by changing the electrons drift velocity. Eventually, all these problems were solved in FTC design.

2. Construction of the FTC detector

2.1. Geometry of FTC layers

Each end cap consists of two identical 1 m diameter layers rotated 90° with respect to one another about the beam axis, to provide track coordinates in two dimensions. Each layer contains 26 modules assembled around the LEP beam pipe. Also, to accept the beam pipe the six central modules are split with common readout, gas and power supply. Consequently, due to the split. The six couples of the modules closest to the beam pipe have their sense wires connected together. This means that electronically each layer contains 20 modules. As is shown in Fig. 1b, the local orthogonal coordinate system of the FTC is rotated by $\phi = 5^\circ$ with respect to the global system of coordinates. This is due to the necessity of accepting the head of the L3 radiofrequency quadrupole (RFQ) target pipe by shortening only one module by 115 mm.

To be integrated into the global coordinate system of L3, each module has special survey marks on both ends of the side walls. The distance between the survey mark's cross and the wire plane was measured with an accuracy of $\pm$ 50 μm. This data was used later as a first approximation in the FTC alignment with physical tracks.

Each of the FTC end caps was covered on both sides with grounded screens of 1.5 mm thick G-10 plates, copper coated on one side. These screens protected the FTC from the influences of surrounding TEC and BGO electronics and other kinds of electromagnetic noise.

2.2. Drift module structure

Fig. 3 presents the scheme of the drift module of FTC. The module contains four signal wires (SW) between field shaping wires (FW) in the median plane. The distance between adjacent wires is 3 mm and there is only 2 mm between the FWs of the edge drift cells and the field shaping electrode walls. Two drift spaces of 22 mm along y are symmetric with respect to the wire plane and bounded by 0.5 mm thick copper-clad fiberglass cathodes. In this geometry, the left–right ($+y$, $-y$) drift ambiguity of the track is always resolved because of the LEP source point constraint. This simplifies resolving the left– right ambiguity of tracks at the module level.

We did not use a special high-resistive wire for charge division purposes. An ordinary 25 μm diameter gold-plated tungsten signal wire with $R_w = 100\ \Omega/m$ was used both for drift time and charge division measurements. This significantly simplified the aging problems of the FTC in comparison with the situations discussed by the authors in Ref. [5]. For the FWs 150 μm beryllium bronze wire was used. The rather big diameter of the FW was chosen to keep the electric field intensity on the surface of the field shaping wire less than 10 kV/cm thus avoiding the possibility of microsparking on the FW surface.

The walls of the module are 1.5 mm thick fiberglass plates with printed field shaping strips on both sides, 0.5 mm wide with a 2 mm period. The strips from opposite side walls with equal potentials are connected with pins on both ends of the module (shown by dashes in Fig. 1b). They cause the uniform electric field in the modules end regions. The precise high-voltage divider provides a uniform electric field with equipotential planes parallel to the median plane and is placed right on the edge of the field-shaping strips of the side wall.

3. FTC readout electronics

Fig. 4 shows the scheme of readout electronics of the FTC. Signals from both ends of each SW are fed to charge-sensitive preamplifiers which are placed directly on FTC modules. Preamplifiers have compact dimensions and a power consumption per one layer equal to 5 W. The amplification coefficient of the preamplifier is about 10. For charge division measurements, the FTC's preamplifier is adjusted to operate as mentioned above with a low-resistive anode wire. The current signal coming from the wire is integrated with integration time $\tau = 200$ ns

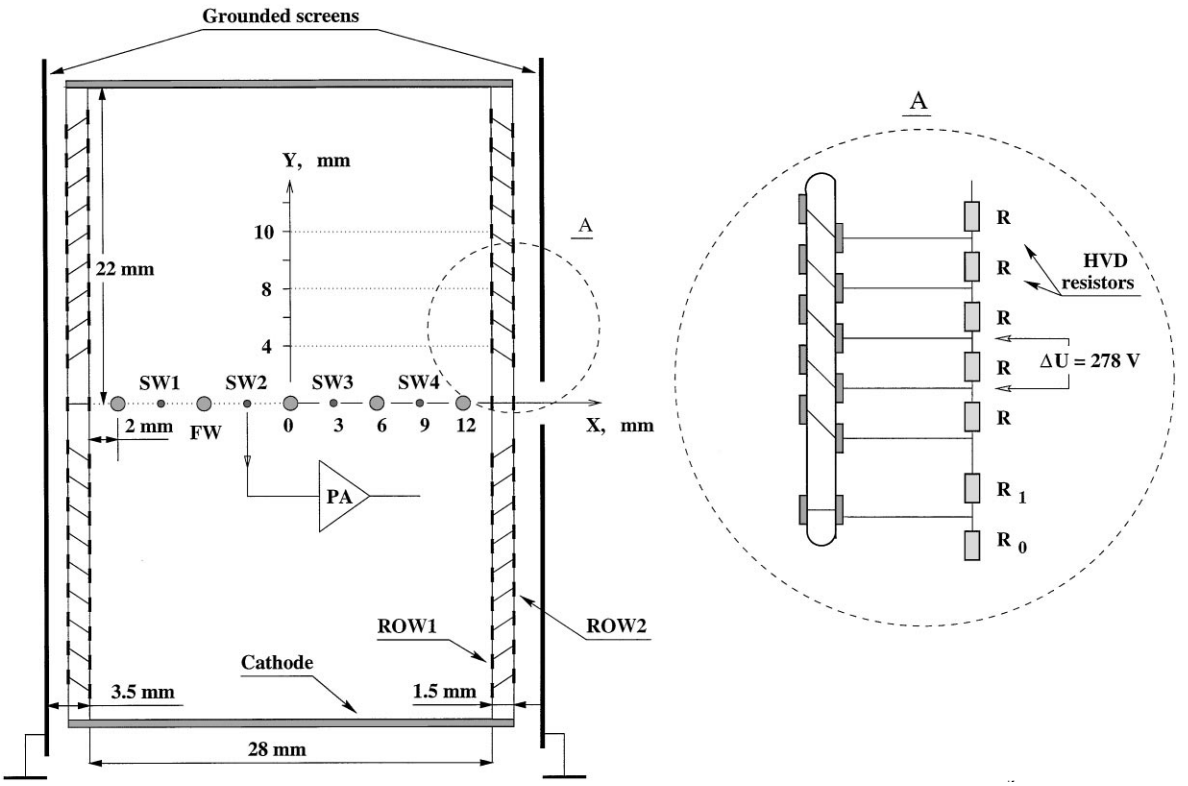

Fig. 3. Cross section of the FTC drift module with the scheme of the HVD divider.

and transported through a twisted pair cable (length about 40 m) to a Shaper Discriminator Card (SDC). The SDC contains both an analog and a digital circuit. The latter takes as input the sum of signals from both ends of the wire. After differentiating with $\tau d = 5$ ns and $1/\tau$ compensation of the ion tail, the signal comes to a discriminator with a variable controlled threshold. This allows to obtain double hit resolution of less than 50 ns. The output signal of the digital circuit has a standard ECL level. The analog circuit is used to separately amplify and shape the signals from both wire ends with "RC = CR" type correction applied at this stage. Both digital and analog signals come to the Demultiplexer and TDC modules. The Demux is a specially designed module which enables to switch the analog signals in a multiple hit event consecutively to different outputs. The fast linear switches driven by the digital signals are opened for a fixed time interval which may be chosen in the range 100–200 ns. For economic reasons, only one SW each drift module is processed in this way.

Each of the half layers is equipped with a transformer which allows to distribute test signals to each of the PA's inputs. The test signals are used for checking the whole electronics chain as well as for calibration purposes.

4. Choice of the wire spacing

4.1. Space resolution and gas gain choice

To satisfy the FTC detector requirement, the gain of the gas mixture should provide both the drift time and charge division measurements. As known, to obtain a good spatial resolution via drift time measurement, the gas gain should be at the level of $G \geq 4 \times 10^4$ [6,7]. The charge division method requires the measurement of the integrated

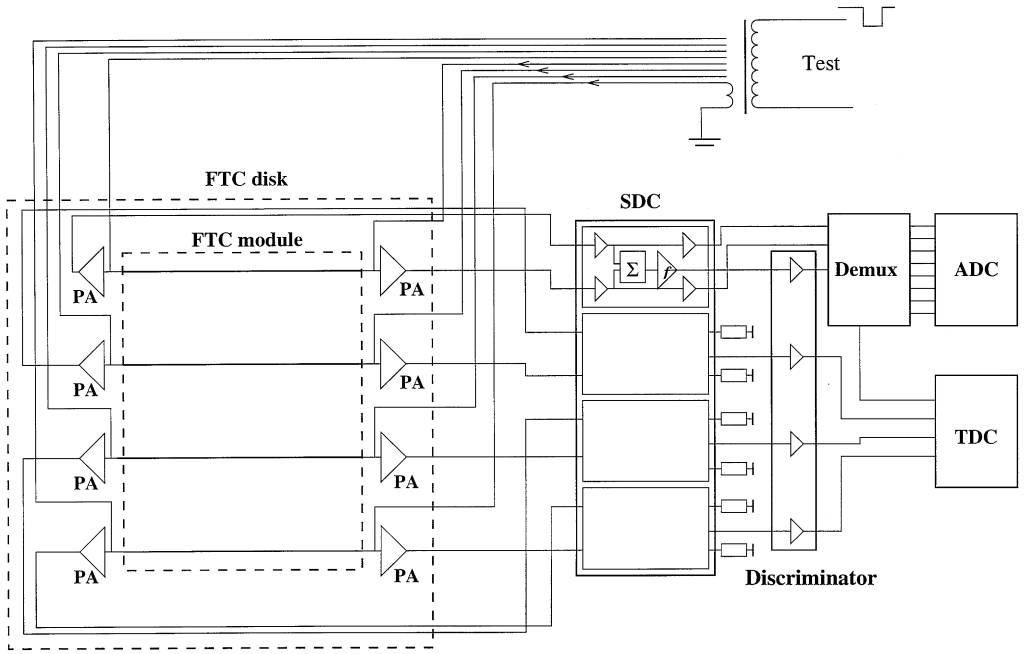

Fig. 4. Schematic diagram of the readout electronics.

charge from each hit at both ends of the signal wires. Then the ratio of the signal amplitudes from the wire to the noise determines the accuracy of the space resolution. Having a rather higher noise for a low-resistive wire, we need a bigger gas gain in the drift chamber. The determination of the track multiplicity for up to 5–7 particles implies in real geometry the charge division space resolution at the level of 2% from the wire length. Hence, the necessary gas gain in our case for the charge division method may be estimated as [8]:

$$\sigma_{\mathrm{CD}} \approx k \frac{2\lambda\rho}{Qs} \tag{1}$$

where k is a coefficient dependent on the impedance of the preamplifier R_{PA} and the wire resistance R_{w}. In our case ($R_{\mathrm{PA}} = 50\,\Omega\mathrm{m}$, $R_{\mathrm{w}} = 100\,\Omega\mathrm{m/cm}$): $k = 1$; $\lambda = 40$–100 cm is the length of the FTC signal wire; $\rho \leq 2 \times 10^4 \mathrm{e}^-$ is the noise level. $Q_S = N \times G$ is the charge collected from both ends of the wire, which is determined by the number of electrons on the charged particle track $N = 60\mathrm{e}^-$ and the gas gain G on SW. It follows from (1) that to have the charge division spatial resolution at a level $\sigma_{\mathrm{CD}}/\lambda \approx 2\%$, the gas gain should be about $G \geq 4 \times 10^4$. Eventually this value defines the required gas gain for the FTC.

4.2. Wire spacing and gas mixture

As is shown in Fig. 3, the free space for the sensitive zone of a module is equal to $\Delta X = 28$ mm. Thus, it would be possible to obtain up to seven drift cells with the width $s = 4$ mm and thereby make the modules spatial resolution via drift time even better than demanded. Nevertheless, the FTC resolution requirement is provided at least by four drift cells with $s = 6$ mm. This is easy to see:

$$\Delta\varphi = \frac{\sigma_{\mathrm{sw}}}{4 \times s} \leq 10\ \mathrm{mrad} \tag{2}$$

$$\sigma = \frac{\sigma_{\mathrm{sw}}}{\sqrt{N_{\mathrm{wires}}}} \approx 100\ \mu\mathrm{m} \tag{3}$$

if the single wire spatial resolution is $\sigma_{\mathrm{sw}} \approx 200\ \mu$m and the number of signal wires is $N_{\mathrm{wires}} = 4$.

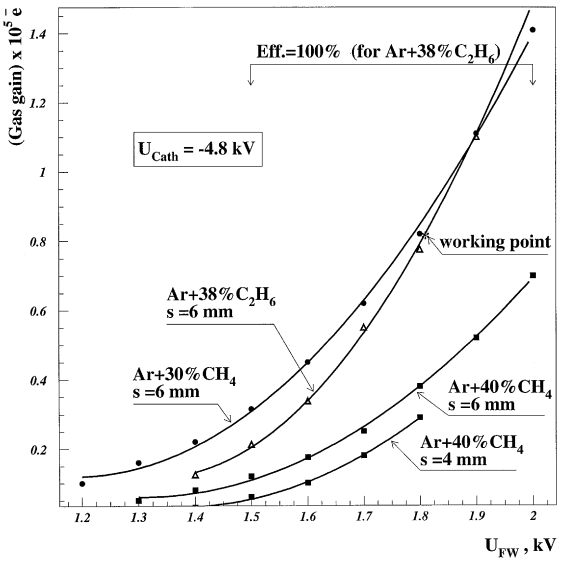

Fig. 5. Gas gain in the different gas mixtures produced by 5.9 keV X-rays from an ^{55}Fe source as a function of the field wire potentials is shown. Two prototype FTC modules with drift cell width $s = 4$ and 6 mm have been investigated.

As mentioned above, to obtain this spatial resolution the gas gain $G \geq 4 \times 10^4$ is sufficient. However, to obtain charge division resolution at the level of 1% from the wire length the gas gain should be twice bigger. Therefore, to choose the anode wires spacing we investigated different gas mixtures with FTC module prototypes.

Two prototype FTC modules with drift cell widths $s = 4$ and 6 mm have been investigated. As a working mixture we used: Ar + 40% CH_4, Ar + 30% CH_4 and Ar + 38% C_2H_6. The gas gain was adjusted through the high voltage applied to the field wires. Fig. 5 shows the gas gain produced by 5.9 keV X-rays from a ^{55}Fe as a function of the field potentials. It is seen that the necessary value of gain can be reached only for the last two mixtures. Clearly, $s = 4$ mm is not apropos for any kind of mixture. Thus, we choose $s = 6$ mm. Thereby the distance between the FW of the outer drift cell and the field shaping electrode in the module is only equal to 2 mm (see Fig. 4) and field shaping strips are placed not at the field wires position as in Ref. [3], but closer. This required the accurate determination of the potentials on the field-shaping strips. To get the desired drift field, the strips must be arranged in space and set to potentials such that the chamber looks infinite. Therefore, the problem of the strip granularity demands very precise choice of one's geometry.

A comparison of the gas mixtures made us reject the methane mixture due to flammability despite the good plateau of drift velocity saturation [9]. The chosen gas mixture, Ar + 38% C_2H_6, is the same used for the L3 muon chambers with one difference – it does not contain the water vapor used in the muon chambers gas. Fig. 6 shows the correspondent "V_{dr}" drift velocity at zero magnetic field and at $B = 0.5$ T obtained using MAGBOLTZ program [10]. The saturation plateau of the drift velocities is seen. At the working range of the field intensity $E = 1.2$–1.4 kV/cm, the electron drift velocity depends on the electric field as

$$|\Delta V_{\rm dr}/V_{\rm dr}| \approx 0.17 \times |\Delta E/E|. \quad (4)$$

Thus in order to minimize the differential nonlinearity of the Y–T relation on the level $|y| \leq 70$ μm, the electric field variation in the drift region should be less than $|\Delta E/E| \leq 2\%$. Such a smooth dependence of "$V_{\rm dr}$" and electrical field intensity decreases the dependence of the Y–T linearity on the electric field deviation. This caused both the mechanical inaccuracies of the module construction and strips granularity by a factor 6.

5. Uniformity of the electric field structure

5.1. Structure of the field shaping strips

To calculate the potentials of the strips, the initial assumption was made that the wire plane consists of an infinite series of grounded SWs, alternating with thicker FWs at a potential $U_{\rm FW} = -1.9$ kV. The field shaping strips are under a potential which corresponds to the value of crossing them equipotential lines and provides the uniformity of the electric field at the distance of 2 mm from the side field shaping electrode wall.

Fig. 7 presents the distribution of the ratio of longitudinal components of the field intensity $E(y)/E_0(y)$ for three versions of strips geometry, where $E(y)$ corresponds to the measured field

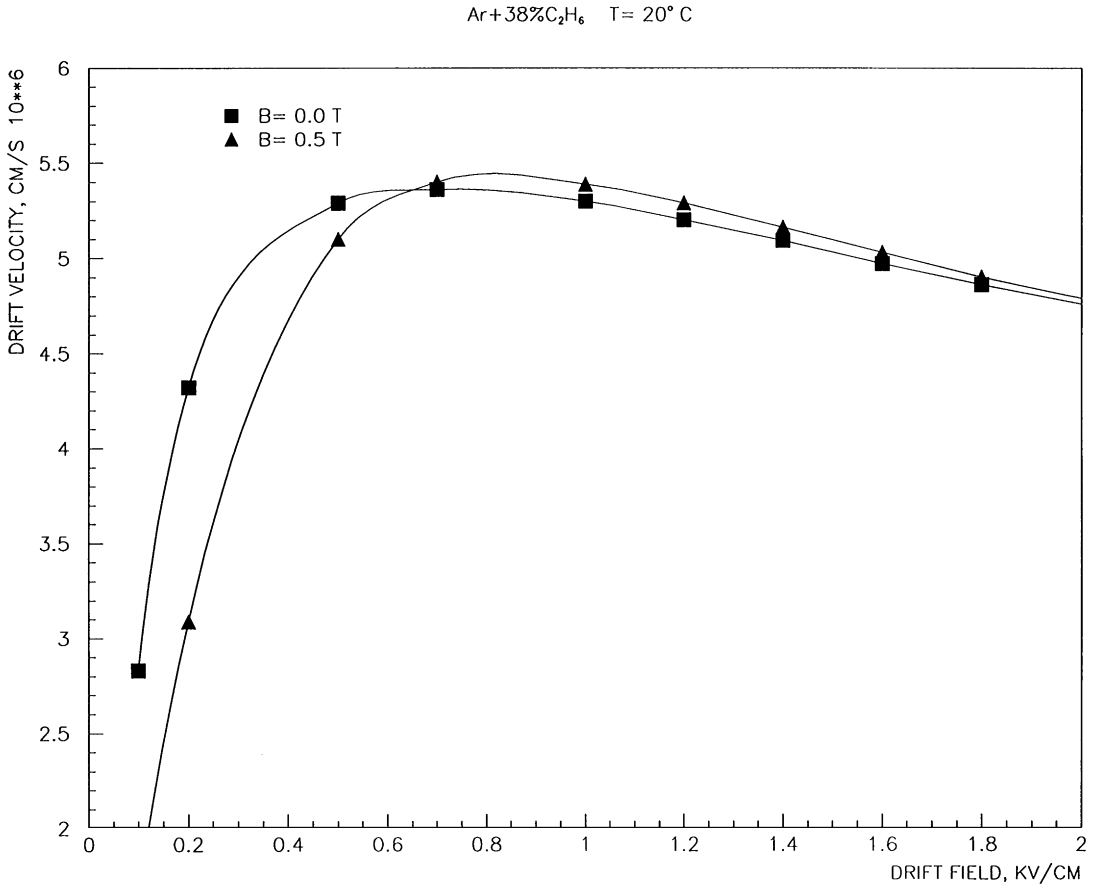

Fig. 6. Drift velocity of electrons in Ar + 38% C_2H_6 gas mixture at zero magnetic field and at $B = 0.5$ T.

intensity and $E_0(y)$ corresponds to the calculated field intensity in infinite geometry without edge effects. It is seen that the step $S_{st} = 2$ mm and the width $a = 0.5$ mm of the strips are optimal both with respect to technology (only 10 strips and the outputs for high-voltage divider) and uniformity of the electric field: $|\Delta E/E_0(y)| \leq 1\%$ at the distance of 2 mm from the wall. Hence the electric field uniformity near the edge drift cells provided by such a strips structure causes $|\Delta v_{dr}/v_{dr}| \leq 0.17\%$.

In the other calculated example ($S_{st} \approx 1, 5$ mm) in Fig. 7, a big difference of field intensity between the strips and on the strips could provoke sparking on the edges of the strips. Therefore, we chose the mentioned geometry of the field shaping strips.

5.2. Electric field structure in the FTC module

As mentioned above due to space limitation the strips of the field-shaping electrodes were placed only at 3.5 mm from the outer protective grounded screen (see Fig. 3). Thus the uniformity of the electric field in such a situation may be distorted. Also it spoils the relationship between drift time and position especially for the outer drift cell. Fig. 8a shows the program simulation of the distorted structure of the electric field in the module. To prevent the grounded screen from distorting the internal field, we placed an additional plane of strips, Row2, between the screen and the original strips, Row1 (see Fig. 3). The additional strips have the same period and potential distribution, but are

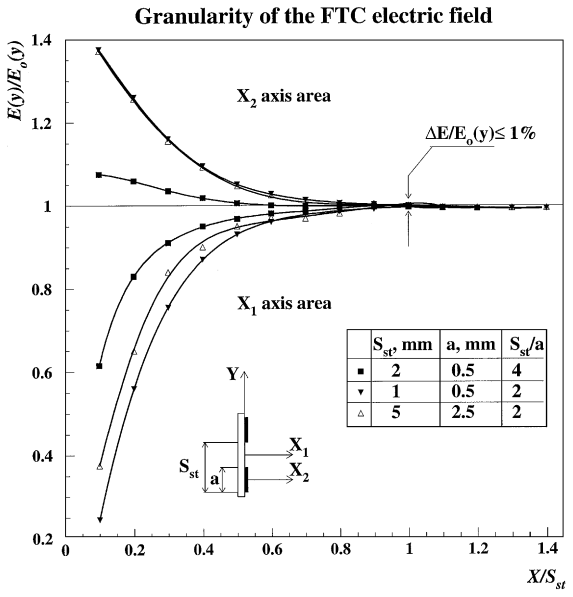

Fig. 7. Distribution of the ratio of longitudinal components of the field intensity $E(y)/E_0(y)$ for three versions of strips geometry, where $E(y)$ corresponds to the current field intensity and $E_0(y)$ corresponds to the calculated field intensity in the uniform electric field of the working drift space.

staggered down by 1 mm with respect to the inside Row1. The method of minimizing these edge effects was discussed in detail in an earlier work [3]. The structure of the electric field in this situation is shown in Fig. 8b. It should be noted that in the entire active volume of the FTC ($|X| \leq 12$ mm and $5 \leq Y \leq 22$ mm) the simulated electric field is uniform within $|\Delta E/E| \leq 0.5\%$ that provides $|\Delta v_{dr}/v_{dr}| \leq 0.08\%$.

5.3. Mechanical imperfections

Electric field uniformity provided by such a strips structure together with a good protection from the external influences on the electric field makes $Y-T$ linearity sensitive only to mechanical imperfections. We estimate the maximum mechanical imperfection of the FTC production as $\Delta_{max} = 50$ μm. This corresponds to a variation of the field intensity at the level of $|\Delta E/E| \leq 1.3\%$ and drift velocity deviation as $|\Delta v_{dr}/v_{dr}| \leq 0.2\%$.

5.4. High-voltage divider

As mentioned above the distribution of potentials on the strips is determined by the electric field structure that is set through $U_{Cath.} = -4.8$ kV cathode potential and $U_{FW} = -1.9$ kV field potential. This provides the field intensity in the drift space equal to $E = 1.38$ kV/cm. Application of the calculated voltage difference to each field shaping strips gap is provided by a specially designed precise high-voltage divider (HVD). The scheme of the HVD is presented in Fig. 3. The calculated values of the HVD resistors are correspondently equal to $R_0 = 19.6$ MΩ, $R_1 = 7.35$ MΩ, $R = 5$ MΩ, which ensure that the voltage drop between the strips of the module $\Delta U_{HVD} = 278$ V. The FTC's divider is realized with the application of high-resistive thick film technology which provides high temperature stability (not worse than 5×10^{-4}) and resistor accuracy at the level 1×10^{-3}. The dimensions of the divider $20 \times 30 \times 0.5$ mm^3 is such that it is appropriate to the FTC layout demands. To minimize the HVD affect from resistors on the electric field to a level $|\Delta E/E| \leq 0.1\%$, the ratio I_L/I_{HVD} of leakage current between strips (I_L) and HVD current (I_{HVD}) should be $\leq 1 \times 10^{-3}$. On the other hand, due to the lack of free space the power consumption of the HVD is limited to $P_{HVD} \leq 0.4$ W. Hence, the dividers current should be chosen between the values:

$$P_{HVD}/U_{Cath.} \geq I_{HVD} \geq I_L \times 10^3. \quad (5)$$

We set $I_{HVD} = 50$ μA which limits the leakage current at the level $I_L \leq 50$ nA.

5.5. Minimizing the surface leakage current

Thus, having a precise and stable HVD, the main problem of the drift module fabrication technology was minimization of the leakage current between the strips. In the production of modules, the fiberglass surface of the field shaping electrodes was often polluted by the solder flux, oil and even by finger prints. Fig. 9a shows the leakage current between the strips on the pattern electrode for different kinds of pollution. Before measuring the current the electrode plate was cleaned by alcohol. It is seen that such cleaning is not sufficient. Especially "dangerous" are traces of solder flux (see

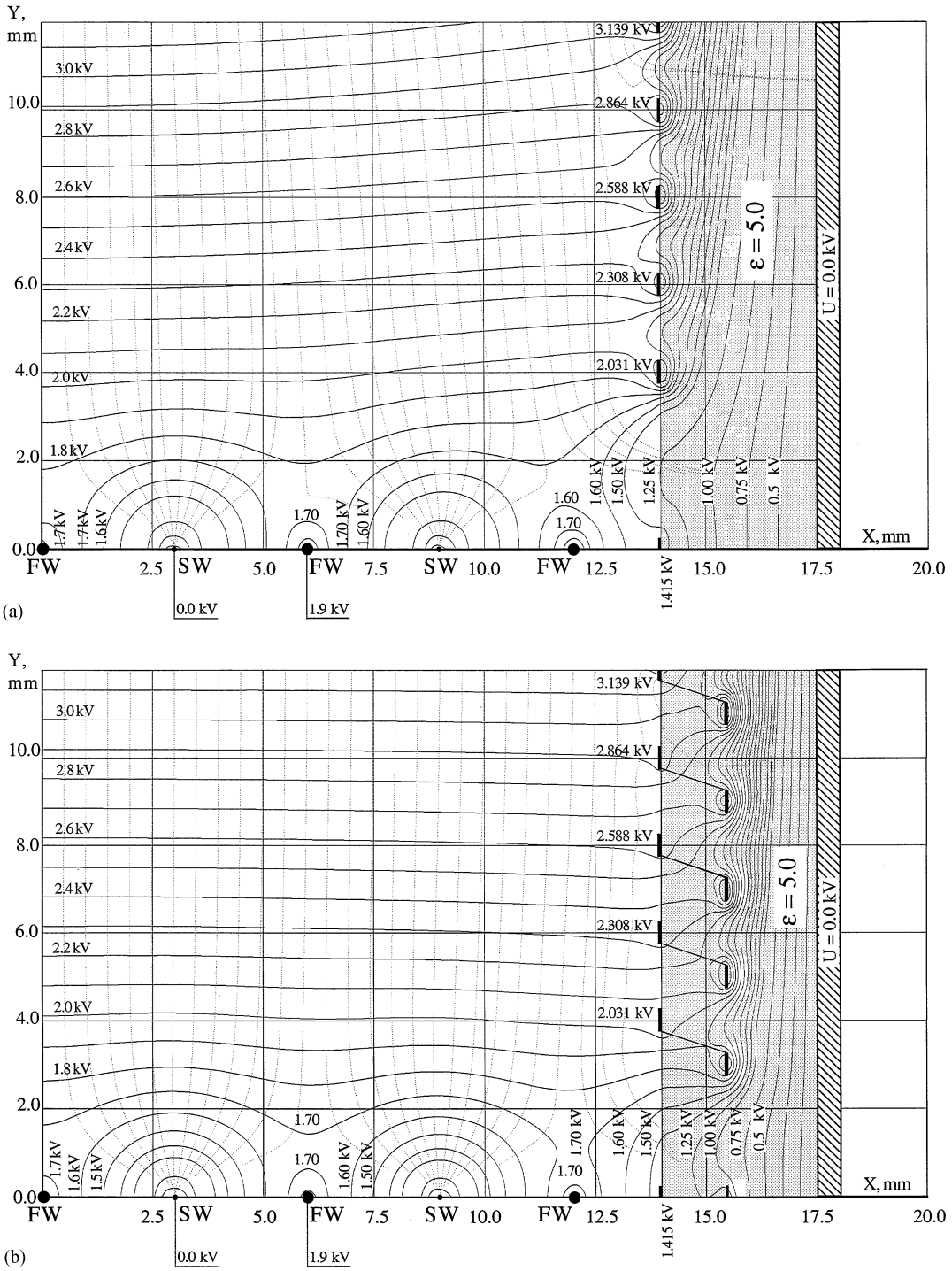

Fig. 8. Program simulation of the structure of the electric field in the FTC module. (a) Electric field structure with single plane of strips (Row1, see Fig. 3) distorted by the grounded screen, and (b) electric field structure protected by the additional plane of strips (Row2, see Fig. 3).

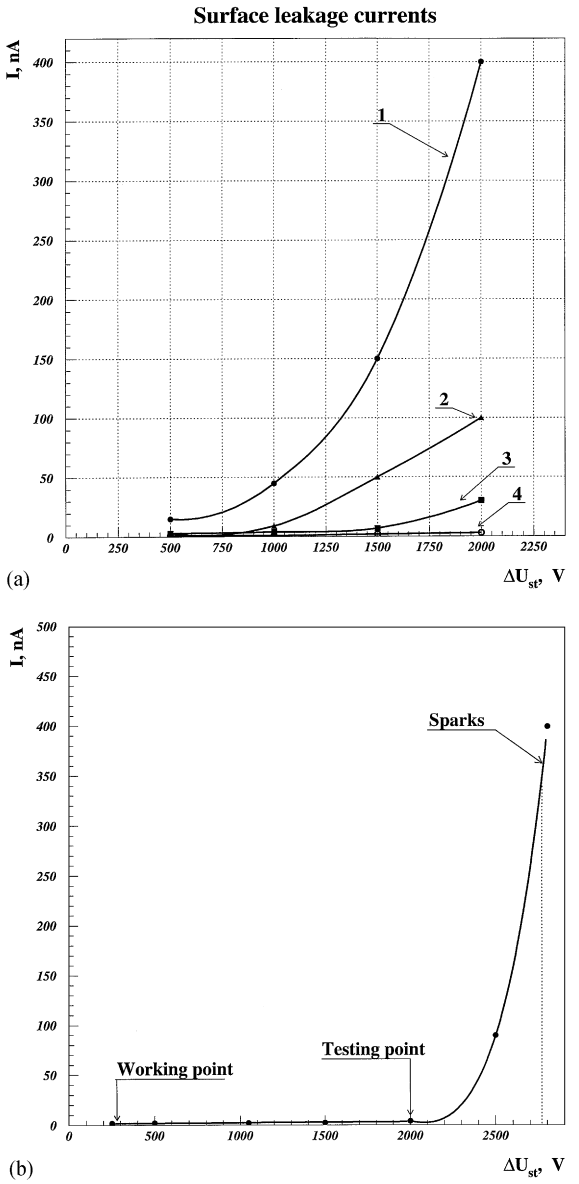

Fig. 9. (a) Leakage current between the strips for different kinds of pollution versus voltage drop ΔU_{st}, where 1 – the traces of solder flux; 2 – traces of vacuum oil; 3 – traces of finger prints; 4 – result of ultrasonic bath cleaning. (b) Dependence of the leakage current on voltage drop ΔU_{st} applied to the neighboring strips on the field shaping electrode.

Fig. 9a, Fig. 1), as they are difficult to clean. Only the ultrasonic bath guaranteed an appropriate quality of cleaning from all kinds of pollution (see Fig. 9a, Fig. 4). After such a cleaning we obtained a maximum of less than 5 nA of surface leakage current between the field shaping strips. Fig. 9b shows the dependence of the leakage current on the applied voltage drop ΔU when the field shaping electrode is cleaned by ultrasound. It is seen that the nonlinear part of the leakage current starts to grow from the point $\Delta U = 2$ kV. Such a voltage drop causes a sharp increase of the leakage current if any pollution appears on the testing electrode. Additionally, since the value $\Delta U = 2$ kV is about 7 times larger than a real voltage drop applied by the divider $\Delta U_{HVD} = 278$ V, it provides a reliable control of needle points on the strip surface. That is why we checked the surface between each pair of the strips at this potential.

Eventually a combination of the high-voltage control and ultrasonic cleaning of the field shaping electrodes provided the ratio of real leakage current ($I_{Real} \leq 5$ nA) and limit leakage current ($I_L \leq 50$ nA), i.e. at a level little more than 10%, that almost eliminates the leakage current influence on the electron drift velocity $|\Delta v_{dr}/v_{dr}| \leq 0.002\%$! Thus the precision of the electric field setting by HVD is determined only by the resistors accuracy $|\Delta E/E| \leqslant 0.1\%$, which corresponds to $|\Delta v_{dr}/v_{dr}| \leqslant 0.02\%$.

6. Temperature distribution on the surface of the FTC

The temperature stability of working gas mixture is an essential requirement for the FTC, because, heat sources (HVD and PA) located on the edges of modules, cause nonhomogeneous temperature distribution along drift modules of FTC. In our case the total power of the HVDs is 30 and 10 W for preamplifiers per layer of FTC. Taking into account both the poor convection conditions in the isolated space of the FTC location and probable influence of the temperature gradient on the electron drift velocity in working mixture Ar + 38% C_2H_6, the heat distribution problem was specially investigated. For this purpose a full-scale mechanical prototype of the two half layers (X,Y) was made. Special resistors were used instead of HVD and preamplifiers to simulate the heat production at the level (HVD – 15 W) and (preamplifiers – 5 W)

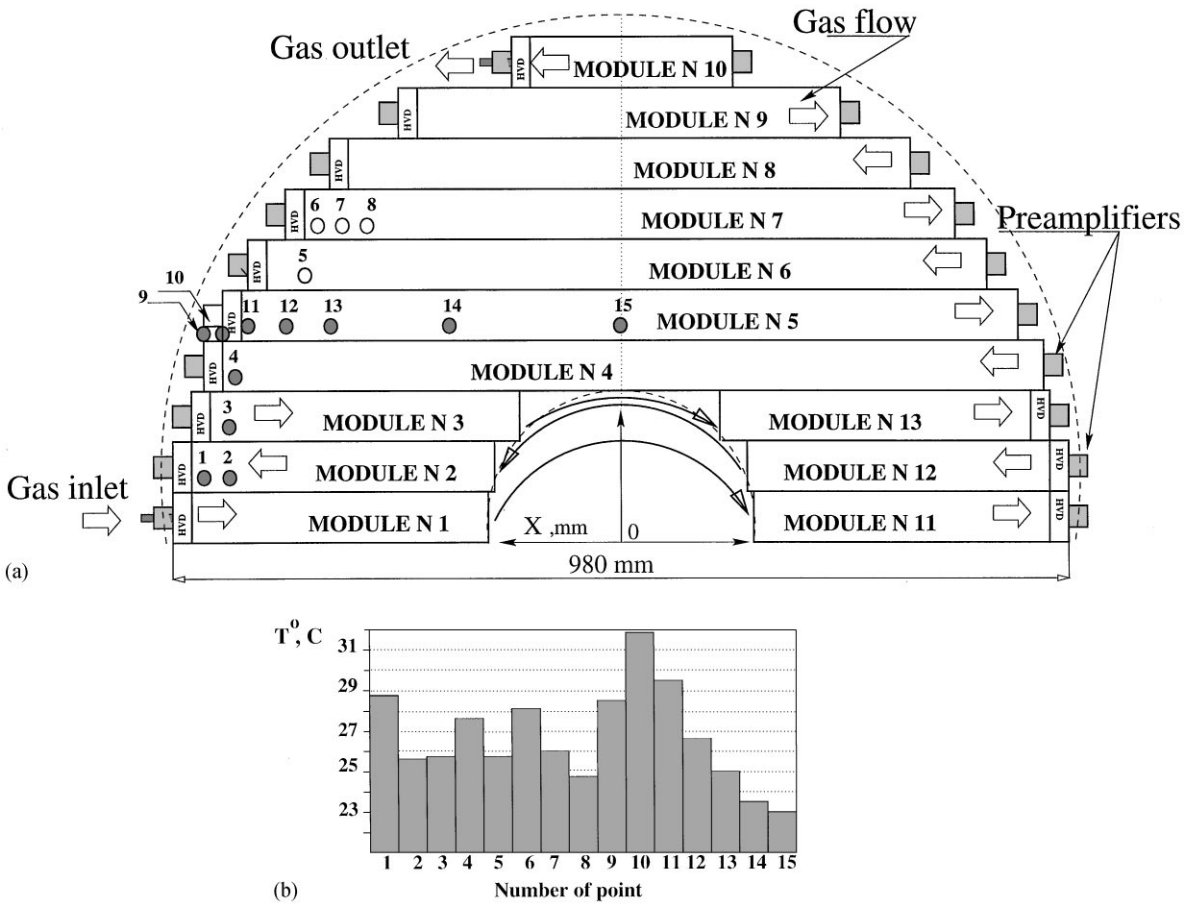

Fig. 10. (a) Schematic view of thermosensitive elements positioning on the mechanical FTC prototype. (b) Saturation temperature after 5 h of the FTC prototype heating in an isolated volume.

for each half FTC layer. On the surface of the prototype were mounted 15 thermosensitive elements. To simulate the real heat exchange the prototype was located in an isolated volume. Fig. 10 shows the positioning of elements and corresponding saturation temperature (after 5 h of heating). As seen in Fig. 10b, point 10 is heated up to 32°C, i.e. about 10°C more than the minimum temperature in point 15. The distribution of temperature along the wires for module numbers 2,5 and 7 has been measured as shown in Fig. 11. It is seen that the temperature is minimized at a distance ~ 250 mm from the edge of the module. To estimate the influence of the temperature gradient on the $Y-T$ linearity, the electrons drift velocity as a function of the electric field for various temperatures namely 23°C and 32°C has been calculated using the MAGBOLTZ program [10]. The temperature gradient $\Delta t^{\circ} = 9^{\circ}$C provokes drift velocity variation $|\Delta v_{dr}/v_{dr}| \approx 0.5\%$. Hence for 22 mm drift path the resulting change of coordinate is equivalent to 115 μm, which is not acceptable.To make the heat distribution along the drift modules more uniform the preamplifiers outputs and the HVD were alternated along the edges of disk layers. As a next step we organized a contrary gas flow by consecutively connecting one module to another, see Fig. 10. This caused heat exchange between the "warm" and "cold" gas flows and provided an almost uniform temperature distribution under real FTC

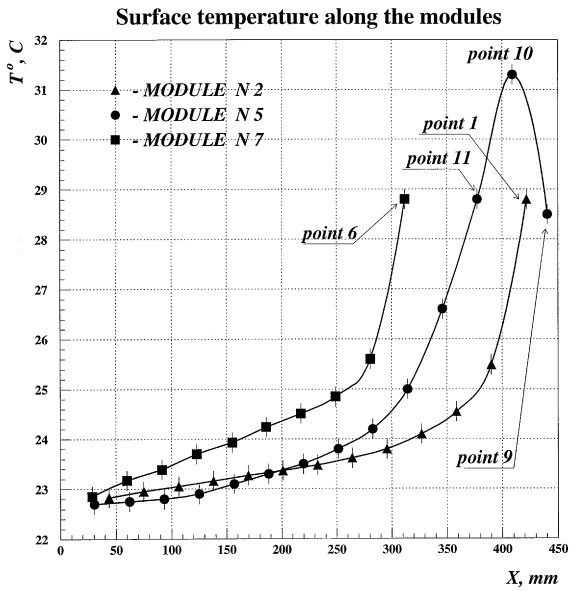

Fig. 11. Distribution of temperature measured along the wires for modules N2,N5 and N7.

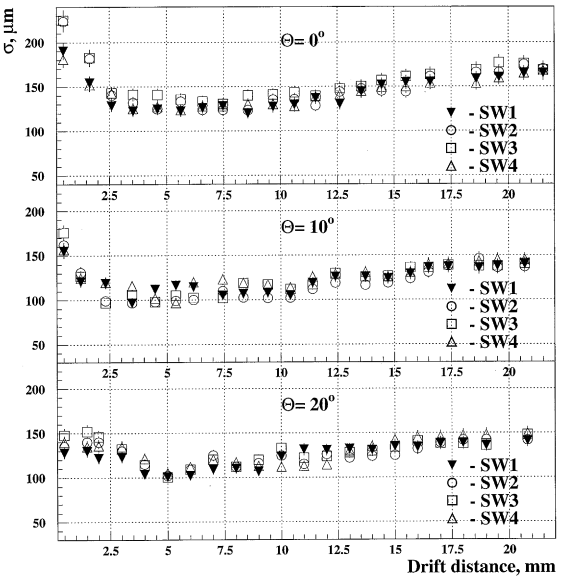

Fig. 13. Spatial resolution as a function of drift path for Θ-angles of the tracks: 0°, 10° and 20°.

conditions at a level $\Delta t^{\circ} = 2^{\circ}$C. Actually, as a result $|\Delta v_{dr}/v_{dr}| \leq 0.1\%$.

In order to keep the temperature stability under control during the experimental run, 16 thermosensitive elements are embedded on the surface of the FTC.

7. Results of FTC tests

Fig. 12 shows the setup for testing with the FTC with a 1-GeV proton beam. We used Ar + 38%C_2H_6 as the working gas mixture in the FTC. The beam monitoring was done by the three proportional chambers with cathode readout, providing the spatial resolution $\sigma_{PC}(x, y) \leq 100$ μm per chamber. This permits us to obtain a spatial resolution per track of about $\sigma(x, y) \approx 90$ μm. To avoid the influence of the multiple scattering effect we obtained the spatial resolution as a least-squares fit for a straight line using proportional chambers and four SWs of the FTC module. The deviation of the measured coordinates by sense wire SW_2 and the fitted line gave us $\sigma(x)$ – the spatial resolution of a single wire. Fig. 13 shows the space resolution as

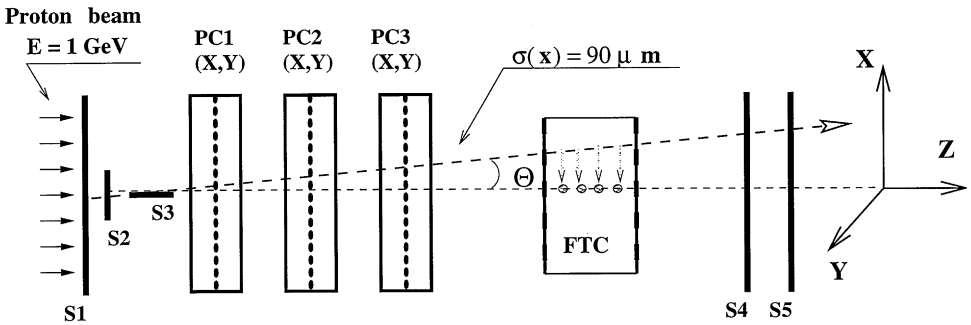

Fig. 12. Scheme of the setup for the FTC test with a 1-GeV proton beam. The beam monitoring was done by the PC1,PC2 and PC3 proportional chambers with cathode readout, providing a spatial resolution $\sigma_{PC}(x, y) \leq 100$ μm per chamber.

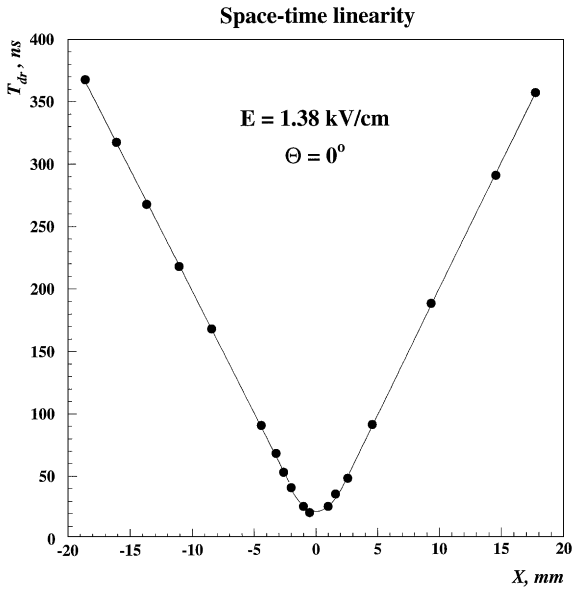

Fig. 14. Space–time relationship measured on the 1-GeV proton beam for the FTC module.

a function of drift length for three Θ-angles of the tracks 0°, 10° and 20°. It is seen that we have, in the working range of the voltage, an appropriate spatial resolution per SW: $\sigma_{sw} < 200$ μm. The space–time relationship measured on the beam for the FTC module is presented in Fig. 14. Eventually, we obtained the linearity of $Y-T$ dependence almost in the whole drift space of the module except for the region close to the wire surface, at about 2 mm width. It appears from the data analysis that differential $Y-T$ nonlinearity is less than 70 μm for $Y \in [2\text{–}22$ mm]. The estimated drift velocity of electrons in this case was equal to $v_{dr} \cong 50.6 \pm 0.1$ μm/ns.

8. Conclusion

1. The end cap detector based on multimodule construction was designed and produced in PNPI for the L3 experiment. The FTC has operated in the L3 experiment for 8 years. Until now we have not seen any signs of deterioration due to ageing.
2. The obtained detector characteristics such as $Y-T$ linearity, spatial and angle resolution satisfy the FTC performance requirements. Thus an approach for solving the problem of interrelated design parameters in the light of external constraints is realized.
3. As a result of this approach the influence of the factors affecting the linearity of $Y-T$ dependence is minimized at the following low levels (for the drift space $Y \in [2\text{–}22$ mm]):

	$\lvert\Delta E/E\rvert$(%)	$\lvert\Delta v_{dr}/v_{dr}\rvert$(%)
Structure of the field shaping strips	1.0	0.17
Protection from the external influences	0.5	0.08
Potentials setting by HVD	0.1	0.02
Maximum temperature variation	—	0.1
Mechanical fabrication imperfection	1.3	0.2

Totally, the nonlinearity of the $Y-T$ dependence in the FTC detector may be estimated as $|\Delta v_{dr}/v_{dr}| \approx 0.3\%$. This corresponds to the maximum error in the measurement of the absolute track coordinate: $|y| \leq 70$ μm.

Acknowledgements

We are very grateful to A.A. Vorobyov (PNPI) for the criticism and fruitful discussions on detectors design. Then we would like to thank the High Energy Physics department of PNPI for approval and use of their facilities. We are indebted to G. Shably and V. Dobyrn for their contribution in the technology of detector production and to V. Sulimov for software help. The authors thank G. Burgers (MIT), M. Lebeau (CERN) and A. Miller (TRIUMF) for their support and useful discussions of the draft.

References

[1] L3 collaboration, Nucl. Instr. and Meth. A 289 (1,2) (1990).

[2] A. Breskin, G. Garpak, F. Sauli, Nucl. Instr. and Meth. 124 (1975) 189.
[3] G.E. Gavrilov et al., Nucl. Instr. and Meth. A 356 (1995) 189.
[4] A. Weltin, Nucl. Instr. and Meth. A 264 (1988) 213.
[5] M. Atac et al., IEEE Trans. Nucl. Sci. NS-34 (1987) 476.
[6] F. Sauli, Nucl. Instr. and Meth. A 273 (1988) 805.
[7] H. Drumm et al., Nucl. Instr. and Meth. 176 (1980) 333.
[8] V. Radeka, IEEE Trans. Nucl. Sci. NS- 21 (1974) 51.
[9] A. Peisert, F. Sauli, Yellow Preprint, CERN 84-08, 1984.
[10] S.F. Biagi, Univ. Liverpool, MAGBOLTZ – Version 2.2.